

Automated classification of plasma regions using 3D particle energy distribution.

Vyacheslav Olshevsky^{1,2}, Yuri V. Khotyaintsev³, Andrey Divin⁵, Gian Luca Delzanno⁴, Sven Anderzén¹, Pawel Herman¹, Steven W.D. Chien¹, Levon Avanov⁶, Stefano Markidis¹

¹KTH Royal Institute of Technology, Stockholm, Sweden

²Main Astronomical Observatory, Kiev, Ukraine

³Swedish Institute of Space Physics, Uppsala, Sweden

⁴Los Alamos National Laboratory, USA

⁵St. Petersburg State University, St. Petersburg, Russia

⁶NASA Goddard Space Flight Center, Greenbelt, USA

Key Points:

- We develop a technique for automated classification of plasma region traversed by the MMS spacecraft
- A three-dimensional deep convolutional neural network classifies observations with 99% accuracy
- Our software could readily be deployed to classify all available data of the day-side campaign

Abstract

Even though automatic classification and interpretation would be highly desired features for the Magnetospheric Multiscale mission (MMS), the gold rush era in machine learning has yet to reach the science done with observations collected by MMS. We investigate the properties of the ion sky maps produced by the Dual Ion Spectrometers (DIS) from the Fast Plasma Investigation (FPI). Running the Principal Component Analysis (PCA) on a mixed subset of the data suggests that more than 500 components are needed to cover 80% of the variance. Hence, simple machine learning techniques might not deal with classification of plasma regions. Use of a three-dimensional (3D) convolutional autoencoder (3D-CAE) allows to reduce the data dimensionality by 128 times while still maintaining a decent quality energy distribution. However, k-means clustering computed over the compressed data is not capable of separating measurements according to the physical properties of the plasma. A three-dimensional convolutional neural network (3D-CNN), trained on a rather small amount of human labelled training examples is able to predict plasma regions with 99% accuracy. The low probability predictions of the 3D-CNN reveal the mixed state regions, such as the magnetopause or bow shock, which are of key interest to researchers of the MMS mission. The 3D-CNN and data processing software could easily be deployed on ground-based computers and provide classification for the whole MMS database. Data processing through the trained 3D-CNN is fast and efficient, opening up the possibility for deployment in data-centers or in situ operation on-board the spacecraft.

1 Introduction

The major objective of the Magnetospheric Multiscale Mission (MMS) (Burch et al., 2016) is to understand the physical processes and the natural sequence of events causing magnetic reconnection, a phenomenon responsible for the release of tremendous amounts of the magnetic field energy in space. This energy is the driver for space weather events, energetic particle outbursts, solar flares, etc.. Hence the ability to identify reconnection events in the data obtained from the spacecraft is vital for the mission's success. The overall amount of data is immense, hundreds of thousands of data samples of different kinds are measured per day. Presently, data pre-selection and analysis involves a lot of human interaction from the scientists-in-the-loop (Fuselier et al., 2016) who continuously browse the data and choose which should be stored and transmitted to the ground, and which should be discarded already on orbit. Same applies to the data centers on the ground, which use a lot of heuristics and visual data inspection by scientists and engineers. Automatization of data classification and interpretation would significantly reduce the amount of manpower needed to process much more data, with the potential for more new discoveries.

The gold rush in Machine Learning (ML) applications to nearly all fields of technology and research, induced by the availability of data and compute resources (LeCun et al., 2015), has yet to make its impact on the space plasma physics. In particular, little to no work is published on application of the ML techniques for the analysis of data from space missions such as MMS. Meanwhile, MMS is now the primary focus of interest of the major part of researchers in the field. The ML techniques have found their application in different areas of space weather research, which is closely related to the space plasma physics. Most of the efforts are rather ambitious in their attempts to forecast various (usually catastrophic) conditions: geomagnetic indices and storms, high-energy particle bursts at geosynchronous orbit, solar flares, coronal mass ejections, and solar wind speed (Camporeale, 2019). Our goal is humbler, instead of predicting new events, we aim at classifying the existing data.

On its path in the dayside campaign MMS passes three well-defined plasma environments: pristine Solar Wind (SW), Magnetosheath (MS), and Magnetosphere (MSP).

The transition between MSP and MS is called the magnetopause (MP), while the SW and MS regions are separated by a rather broad Ion Foreshock (IF). This region contains a mixture of reflected ions, SW, and MS plasmas. A narrow bow shock separates it from the MS. Boundaries between the plasma regions are not stationary, they are affected by the varying solar wind conditions. Boundary detection is most crucial for the scientific goals of the MMS mission, as the dayside magnetic reconnection is believed to occur in the MP layer (Fuselier et al., 2017). Piatt (2019) developed a technique for automated detection of the MP using a statistical hierarchical Bayesian mixture model based on the data derived from measurements of several instruments on MMS. It employs time dependence of the data and needs data pre-processing for computing the derived quantities to estimate how likely each measurement is a MP. The evaluated accuracy of this single-class model is 31% true positive rate and 93% true negative rate.

We have developed a simple and robust technique for automated detection of four plasma regions (SW, MS, MSP, IF) using only the ion energy distributions. This multi-class model classifies individual measurements (hence it does not use any time history of the data), and, as we will show later, its estimated accuracy is 99%. The method is ready to be deployed for data processing in data centers. In this paper, we present the results of our study of the data available from the dual ion spectrometers (DIS) from the Fast Plasma Investigation (FPI) suite (Pollock et al., 2016). The discriminative analysis was conducted with the use of different ML techniques including the Principal Component Analysis (PCA), Convolutional Autoencoder (CAE), and Deep Convolutional Neural Network (CNN). We describe the data in section 2, introduce the methods in section 3, and present our results in section 4.

2 Data

The FPI DIS data has been taken from the MMS data archive¹ and represents the level-two data product of FPI, namely the ion energy distribution. Each sample is a [32, 16, 32] array, where the dimensions correspond to 32 energies, 16 polar angles and 32 azimuthal angles. The spacecraft coordinate system is close to GSE. Measurements are taken with a 4.5-sec interval and saved in NASA’s Common Data Format (CDF)². Each CDF file contains no more than 2 hours of observations, or 1600 measurements. Each measurement is uniquely identified by the index of the spacecraft and epoch. Epoch is the moment of time when the data has been taken, in nanoseconds since the standard J2000 moment.

Examples of typical measurement for the dayside campaign are shown in Figure 1. In the plots, a volume rendering of the logarithm of the ion phase space density as a function of energy is shown for four typical examples of: the solar wind, ion foreshock, magnetosheath, and magnetosphere. It looks like existing ML-based image/object recognition techniques would be capable of distinguishing between these regions. Indeed, SW is represented by a narrow beam in the middle of the box (a small ‘ball’ in the representation shown in Fig. 1a). IF is distinguished from SW by the presence of reflected ions or magnetosheath plasma, hence a ‘halo’ around the SW beam in Fig. 1b. The MSH regions are distinguished by the presence of high-energy ions and a large spread in velocity directions (a ‘melon’ in Fig. 1c). Finally, MSP is characterized by isotropic distribution of high-energy ions (Fig. 1d).

¹ <https://lasp.colorado.edu/mms/sdc/public/about/browse-wrapper/>

² <https://cdf.gsfc.nasa.gov>

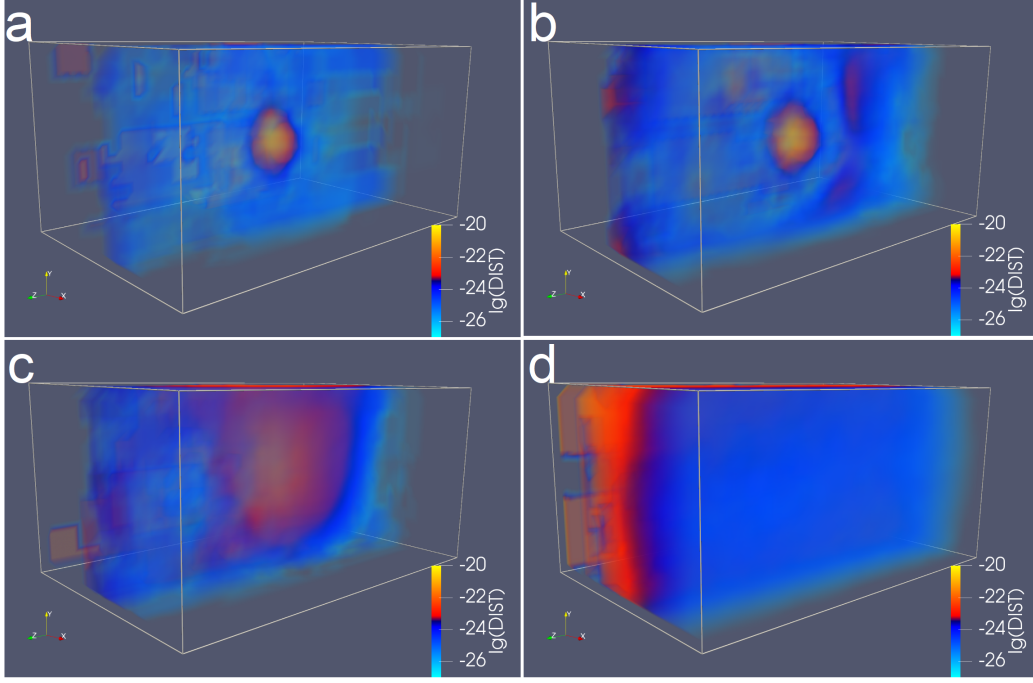


Figure 1. Volume rendering of the logarithm of the ion phase space density for four typical observations. In each panel, x corresponds to the energy bin, y to θ , and z - to ϕ . a) Solar Wind; b) Ion foreshock; c) Magnetosheath; d) Magnetosphere.

Table 1. Human-labelled Dataset

Label	Region	# examples	percentage
-1	Unknown	64,173	23.1
0	Solar Wind	117,441	42.2
1	Foreshock	12,686	4.6
2	Magnetosheath	64,551	23.2
3	Magnetosphere	19,259	6.9
	Total	278,110	100

2.1 Human-labelled dataset

Prior to experimenting with data we have prepared a reference dataset which could be used for evaluation. We have labelled each measurement taken by the DIS on MMS1 during the dayside campaign in November 2017 with one of five classes: -1 - Unknown; 0 - Solar Wind; 1 - Ion foreshock; 2 - Magnetosheath; 3 - Magnetosphere. For labelling, we also used information from other instruments such as the Fluxgate Magnetometer, FGM (Russell et al., 2016). A dedicated software has been developed to help interactively label intervals that belong to the same class. The resulting reference labelled dataset of 278,110 examples is summarized in Table 1. Typical examples of different classes are shown in Figure 1. Some kinds of plasma environment, such as bow shock or magnetopause, could not be classified as belonging to one ‘clear’ class. Any kind of complex mixture or unclear situation was labelled as -1 - Unknown. Actually, these regions, and their statistical properties are most interesting for the researchers because magnetic reconnection happens in these mixed or boundary regions.

Table 2. Training Dataset

Label	Region	# examples	percentage
-1	Unknown	0	0
0	Solar Wind	12,135	42.4
1	Foreshock	7,351	25.7
2	Magnetosheath	7,009	24.5
3	Magnetosphere	2,146	7.5
Total		28,641	100

2.2 Training data

The spacecraft spend long time (tens of minutes) in each plasma region with a similar plasma environment, and rather quickly traverse the transition regions. Therefore a lot of examples belonging to the ‘clear’ classes such as SW or MS are very similar to each other, which was confirmed by computing the Euclidean distances between different examples and a visual inspection of the data. Different classes in the human-labelled dataset (Table 1) are not equally represented, with SW being the most abundant one, and IF being the rarest one. Our early efforts to classify the data using deep convolutional neural network have shown that it quickly trains to accurately classify the SW and MP examples, but often fails on MS and, especially, IF. We have found satisfactory results when a small subset ($\sim 10\%$ of all examples) with a large enough representation of IF samples was used for training. Higher fraction (20%) of training examples neither improves the accuracy evaluated on the test subset, nor the accuracy evaluated over the whole human-labelled dataset.

Results presented in this paper have been obtained with a training set of 28,641 examples randomly chosen from the human-labelled dataset (section 2.1). We have randomly selected 50% of IF, 10% of MS and MSP, and 5% of SW examples from each CDF file (but not less than 100 examples per file) for November 2017 observations (the human-labelled dataset). This way, IF has higher weight in the train set as compared to the human-labelled dataset, while other classes contribute a similar percentage (Table 2). Note, however, that during different months the spacecraft spends different fraction of time in each region, therefore it is yet unclear what is the best combination of training examples, except that IF has to be well represented.

2.3 Data normalization

As we already mentioned, each data example (ion energy distribution) is a [32, 16, 32] array of 32-bit floats. Some values in the array could be 0 (zeros) when no counts have been detected in the corresponding energy/angle bins. Power measured at different energy levels (and for different velocity directions) varies by the orders of magnitude, hence it is adequate to work with the logarithmic representation of the data. But prior to taking the logarithm, each zero-value in the array has to be adjusted. We replace each zero value with the minimum non-zero value in this example. Finally, the x axis of the co-ordinate system of the detector is directed towards the Sun, hence the solar wind beam is spread between the smallest $\theta \approx 0$ and the largest $\theta \approx 2\pi$. It is more convenient to roll each 3D array along the θ dimension so that the SW beam appears in the middle of the array. To summarize, the following procedures were applied to each data sample prior to doing any analysis:

1. Replace all zeros with the minimum non-zero value,
2. Compute \log_{10} ,

3. Subtract the minimum value,
4. Divide by the maximum value,
5. Roll along the last axis (θ) by 16, to put the solar wind beam in the center.

For the PCA (section 3.1) only steps 1 and 2 were applied. For the CAE (section 3.3) only steps 1, 2, and 5 are applied. We tried training our 3D-CAE with all the above steps applied to find the same learning rate and resulting error. However, it is inconvenient to reproduce the input (images) when the data has been normalized.

3 Methods

Current work does not pretend to give a comprehensive study of the efficiency of various ML algorithms used to classify DIS observations. Instead, it proves that supervised learning with 3D-CNN allows precise automated classification, and provides some insight why simpler methods might not be suitable for the task. First, the PCA is used to show that data dimensionality reduction to just a few components can not represent the data satisfactorily. Hence, simple ML techniques might not be able to deal with the classification problem. Second, we demonstrate how a 3D-CAE could be used in conjunction with k-means clustering to classify the data in unsupervised way. However, we were not able to obtain satisfactory results using unsupervised methods, and more studies are needed in this field.

3.1 Principal Component Analysis

The principal component analysis, commonly referred to as PCA was invented in the last century by Pearson (1901); Hotelling (1933). Most comprehensive modern description of the method is given by Jolliffe (2002). The PCA offers a computationally light opportunity for multivariate analysis and visualisation of high-dimensional data. Given a set of n measurements for (a large number of) p random dependent variables, it finds Principal Component (PC) vectors of sizes p . PCs form an orthogonal basis for data that helps in explaining the variance in data in the way that the first PC accounts for the largest possible variance, the second PC accounts for the second largest possible variance, and so on. Essentially each PC is an eigenvector of the $p \times p$ covariance matrix. Each measurement, a point in p -dimensional space, could be projected onto the PCs. As will be shown later, the projections are particularly useful for a simplified graphical representation of the complex datasets.

There are plenty of implementations of the method in different programming languages and platforms. We have used the one from the scikit-learn Python library³. Given a 2-dimensional $n \times p$ array as an input, this class can compute the specified number of PCs and return the reduced-dimensional data transformed into the basis of PC vectors, e.g. an array of $n \times 2$ if only 2 first components are of interest. This array contains the ‘projection’ of each n -size measurement vector on the first 2 PC basis vectors containing most variance of the dataset.

3.2 K-means clustering

K-means clustering is a technique for partitioning an input set of p -dimensional observations into k clusters, where each observation belongs to the cluster with the closest mean value. By indexing clusters one could map a set of vectors to the set of integer numbers, i.e., classify the observations. The algorithm has a high (NP) complexity, and has high memory demand, therefore it is not possible to readily apply k-means to

³<https://scikit-learn.org/stable/modules/generated/sklearn.decomposition.PCA.html>

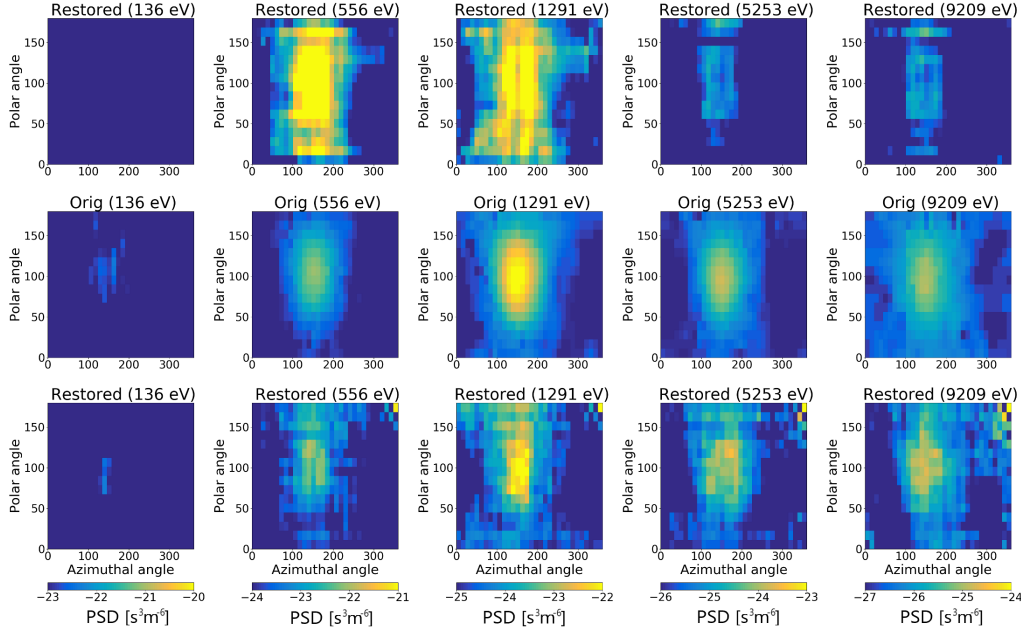


Figure 2. Application of autoencoders to an example from the magnetosheath. Middle row: \log_{10} of energy distributions over ϕ , θ in different energy channels. Top row presents energy distribution restored by 2D-CAE, and bottom row presents the distribution restored by the 3D-CAE.

the datasets considered in this work. We apply k-means to the compressed representation given by the autoencoder (section 3.3).

3.3 Convolutional autoencoder

An autoencoder is a neural network approach to unsupervised learning of data representations with higher or lower dimensionality than the original space, depending on the configuration of the hidden layer. According to Goodfellow, Bengio, and Courville (2016), autoencoders were already used in nineteen-eighties, for instance by Ballard (1987), and although they were probably invented before that, no earlier literature citation was found. Autoencoder is essentially a neural network which first reduces the dimensionality of the input, and then increases it to the initial size. It is trained to minimize the difference between the input and the output (e.g., the mean-squared error, MSE), thus to reproduce the input itself. The smallest fully-connected layer in the middle of the autoencoder is called the bottleneck. It contains the compressed representation of the input. The part of the network before the bottleneck is usually referred to as the encoder, and the part after it is called the decoder.

The motivation to use a convolutional autoencoder, i.e., an encoder with convolutional layers, comes from the successful initial tests of the supervised learning with 3D-CNN. At first, we tried to employ a very simple 2D-CAE commonly used in image processing⁴. However, visual inspection of the encoded-decoded examples was not satisfying, and we have designed a 3D-CAE in which the encoder layers mimic the 3D-CNN used for supervised learning (section 3.4). CAEs are trained to reproduce the input data,

⁴ <https://towardsdatascience.com/deep-inside-autoencoders-7e41f319999f>

hence, they should be able to reproduce the input data as illustrated in Figure 2, where the middle panels represent the input data (skymaps in different DIS energy channels measured in MS), while the upper and the lower panels show the outputs of the 2D-CAE and 3D-CAE, respectively. In the case of the MS and other regions (not shown here) the output of the 2D-CAE is less convincing than the output of the 3D-CAE. Note, that these arguments are not discouraging the usage of 2D-CAEs for the MMS data classification, they just explain our motivation to focus on the 3D-CAE.

In the following, we present the results obtained with the autoencoder built of 8 layers:

1. 3D convolutional with (5, 3, 5) filters with strides (2, 1, 2) and no padding;
2. 3D convolutional with (3, 3, 3) filters with strides (1, 1, 1) and no padding;
3. 3D max-pooling;
4. Fully-connected layer with 128 elements (the bottleneck);
5. Fully-connected with 4096 elements;
6. 3D convolutional with (3, 3, 3) filters with strides (1, 1, 1) and ‘same’ padding;
7. (2, 2, 2)-times Upsampling;
8. 3D convolutional with (2, 2, 2) filters with (1, 1, 1) strides and ‘same’ padding.

In the above, the notation (i, j, k) defines the extent of the filter window or the stride in each dimension. The strides define the steps at which the filter window is moved through the 3D data example. At each position, a convolution of the filter with the input array elements is computed, producing the corresponding element of the input to the next layer of the network. The filter weights are the parameters to be learnt by the CAE.

3.4 Convolutional Neural Network

As noted above, our work is motivated by an apparent success of data classification based on the supervised learning with a CNN. In this strategy, a convolutional neural network (CNN) is fed with a set of examples and human-defined labels. The network is trained to output the corresponding label for each input example. Presently, most impressive results in image classification and feature detection have been obtained by CNNs (LeCun et al., 2015), however there is no ‘universal’ architecture which is proven to be best for different tasks and datasets. Taking into account a 3D nature of the data samples, it felt natural in our case to employ a 3D-CNN rather than 2D-CNNs typically used in image processing. We have developed a new 3D-CNN inspired by the VoxNet architecture proposed by Maturana and Scherer (2015) for object recognition in voxel arrays produced by robotic vision detectors. It consists of 5 layers:

1. 3D convolutional with (5, 3, 5) filters with strides (2, 1, 2) and no padding;
2. 3D convolutional with (3, 3, 3) filters with strides (1, 1, 1) and no padding;
3. 3D max-pooling;
4. Fully-connected layer with 128 elements;
5. Fully-connected layer with the number of elements corresponding to the number of classes (4 in the context of this paper).

The sizes of the filters and the strides were chosen to gradually decrease the size of the voxel array and increase the number of channels, a common practice in image processing. The network has been trained using Adam optimizer with the following parameters: $\beta_1 = 0.9$, $\beta_2 = 0.999$, with a categorical cross-entropy loss function. Given an input example, the CNN outputs a set of probabilities for this example to belong to each of the four classes: SW, IF, MS, MSP. These probabilities sum to 1, and when one of the values is large, it could be considered a clean prediction (not necessarily accurate though).

While if two or more classes have a similar probability, most likely, the example represents a mixed state.

3.5 Implementation and experimental environment

The 3D-CNN and CAEs have been implemented in Python, using Keras⁵ with TensorFlow⁶ backend, all being open source software freely available for users. For training, we used one NVIDIA GTX 1080 GPU with 8GB memory. It takes a few hours to train our CNNs on the training dataset (Table 2) for hundreds of epochs.

For computing PCA and k-means we used the open-source scikit-learn library⁷. PCAs for large datasets were computed on a dedicated machine with 64 GB of RAM.

For reading/writing CDF files we have used the open-source cdf⁸ module.

We have developed a software package in Python 3.6 which could be installed on all operating systems (given all dependencies are satisfied) and be used for classifying, visualizing and analyzing the data. It works with the original folder hierarchy of the MMS data center. The software is hosted in the Bitbucket Git repository⁹. Because the software is still in a pre-release form, it is only available by request, but we plan to release it open-source.

4 Results

4.1 PCA: Results

We have applied PCA to the human-labelled dataset (Table 1) which represents observations of Nov 2017, and to all data collected in Dec 2017 (a holdout dataset). It appears that the first two PCA components represent almost half of the explained variance for each month (1st component – 40%, 2nd component – 9%), but one needs at least 540 PCs to cover 80% of explained variance. Hence, a simple ML technique might not be able to deal with classification of such data. The choice of four categories to classify different plasma regions seems rational, as most examples with the same human-made label tend to cluster together in the PCA diagram shown in Fig. 3a. However, there is no clear separation between different clusters (‘islands’) in the plot: only 2 PCs could not be used to distinguish between different plasma regions. The SW and IF clusters heavily overlap; there is no clear separation between the IF and MS islands.

Interestingly, there are two SW clusters, and two MS clusters. This splitting is not physical, it is due to no counts detected at high energies in colder plasma regions. Figure 4 illustrates that, in the absence of counts at high energies, both PCA components are lower, but when the signal is available, they jump. As will be shown later, this is not important for the high-precision classifier, the 3D-CNN, as it deals with missing data in some bins just fine. This behavior could be further understood from the visualization of the first two PCs shown in Figure 5, where the PC vectors are reshaped back to the shape of data examples, $32 \times 16 \times 32$. The first PC is most sensitive to the counts detected at high energies, and is almost isotropic. The second component is sensitive to the signal at the highest and the lowest energies. Therefore the dimensionality reduction offered by the first two PCs omits very important variance in the center of the energy distribution array.

⁵ <https://keras.io>

⁶ <https://www.tensorflow.org>

⁷ <https://scikit-learn.org>

⁸ <https://github.com/MAVENSDC/cdflib>

⁹ <https://bitbucket.org/volshevsky/spaceml>

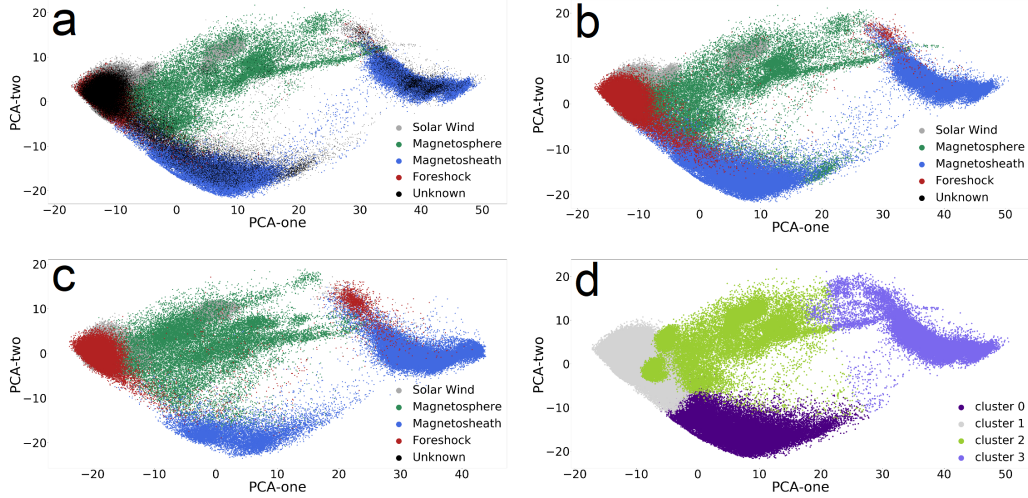


Figure 3. Projection of the data on the two first PCs: a) the human-labelled dataset projected on the PCs computed for this dataset; b) same as (a), but colored according to labels given by the CNN; c) CNN-labelled data for Dec 2017 projected on the PCs computed for Dec 2017; d) same as (a,b), but colored according to the indices of the k-means clusters computed over the compressed representation produced by the encoder part of the 3D-CAE.

The PCA applied to the Dec 2017 data is similar, as illustrated in Figure 3bc, where the data for each month is projected onto the first two PCs and colored according to the labels predicted by the CNN. Apparently, in December there were fewer observations with low signal at high energy bins, resulting in the depletion of the ‘lower left island’ of MS examples. In summary, the first two PCs represent almost 50% of the explained variance in the data, and the dimensionality reduction offered by them is not capable to clearly separate different plasma regions.

4.2 Autoencoder: Results

We have trained the 3D-CAE for 1000 epochs on 90% of examples from the training dataset (2). During training, the MSE has decreased from 327 to 1.7. In comparison, the mean of the absolute value across all dimensions and samples in the train subset is $\langle |X_{train}| \rangle = 26.56$. The autoencoder is interesting for us in two aspects: classification of data from the compressed representation and anomaly detection.

First, an automated clustering algorithm, such as k-means, applied to the compressed representation, provides data classification. The bottleneck layer of the 3D-CAE reported in this paper (section 3.3) has 128 elements. We used the output of this layer (the encoder) as new data representations that we subsequently subjected to clustering with k-means, where $k = 4$ corresponds to the number of classes in the human-labelled dataset. These clusters are used for color-coding the data points plotted in the PCA projection in Figure 3d. Although the clusters computed in this way are well separated in the diagram, they do not reflect the physics-based separation given by human labelling.

Second, the MSE computed between the input and the restored data could be used for anomaly detection. I.e., if the restored data is too different from the input data (for the autoencoder trained on the ‘clean’ examples), it could indicate an anomalous region such as MP or bow shock. Unfortunately, we have not found a clear correlation of the higher MSE with anomalous or mixed plasma states. For example, in Figure 6 multi-

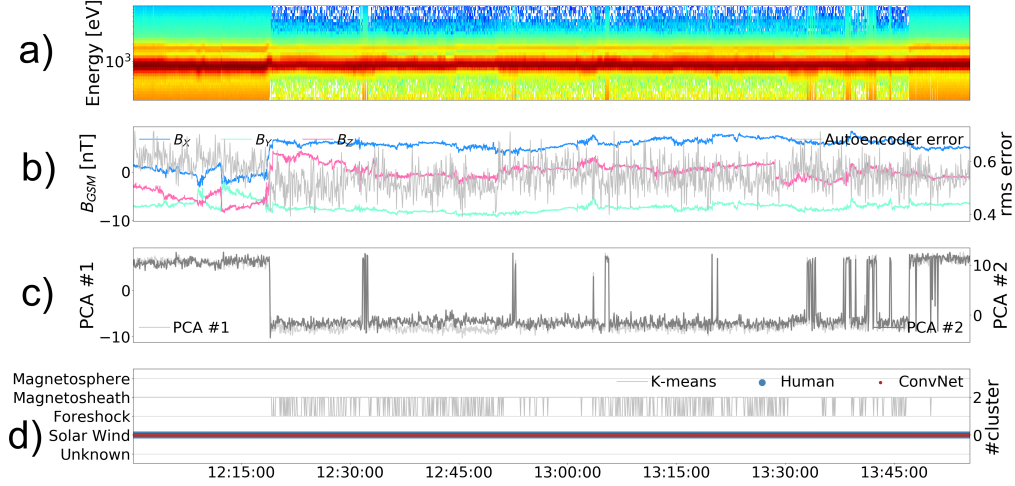


Figure 4. Observations on 2017.11.15 12:00 – 14:00. a) \log_{10} of the energy distribution integrated over ϕ , θ . White pixels at high energy indicate no counts detected at higher energies in the colder solar wind which we replace with a very small value. b) Left axis, blue, green, red: $B_{x,GSM}$, $B_{y,GSM}$, $B_{z,GSM}$; right axis, light grey: rms error of the autoencoder. c) Left axis, light grey: projection of the data on the first PC; right, axis, dark grey: projection of the data on the second PC. d) Human-made labels (blue circles) and classification results: red circles – CNN, grey line – index of the k-means cluster computed over the data compressed by the encoder.

Table 3. CNN error on the reference dataset.

Label	Region	Human-labelled	predicted	Mislabelled	False predictions
0	Solar Wind	117,441	116,978	0.57%	0.17%
1	Foreshock	12,686	13,254	1.74%	5.95%
2	Magnetosheath	64,551	64,446	0.20%	0.03%
3	Magnetosphere	19,259	19,259	0.01%	0.01%
	Total	213,937	213,937	0.47%	0.47%

ple transitions between SW, IF, and MS regions are observed with no prominent jump seen in the autoencoder error. We did not perform a comprehensive study of the results given by the autoencoder on, e.g., the size of the bottleneck layer or the autoencoder architecture. The results presented here serve as illustrative examples which could be used as a motivation for future studies.

4.3 CNN: Results

For supervised learning, the training dataset (Table 2) has been divided into two equal parts: the train set and the test set. We have tried different non-varying learning rates in the range $10^{-7} \leq \alpha \leq 10^{-4}$. The results presented in this paper correspond to $\alpha = 5 \cdot 10^{-7}$ which offers a good balance between the learning speed and accuracy. At this rate, the accuracy on the test set reaches 99.18% in 500 epochs. We present the results of evaluation of the CNN on the whole human-labelled dataset (Table 1) in Table 3. The overall error of the CNN is only 0.47%: it is perfect at detecting MSP, and is very accurate at detecting SW and MS regions. However, almost 6% of the predicted IF regions are false predictions. The confusion matrix given in Table 4, which lists the

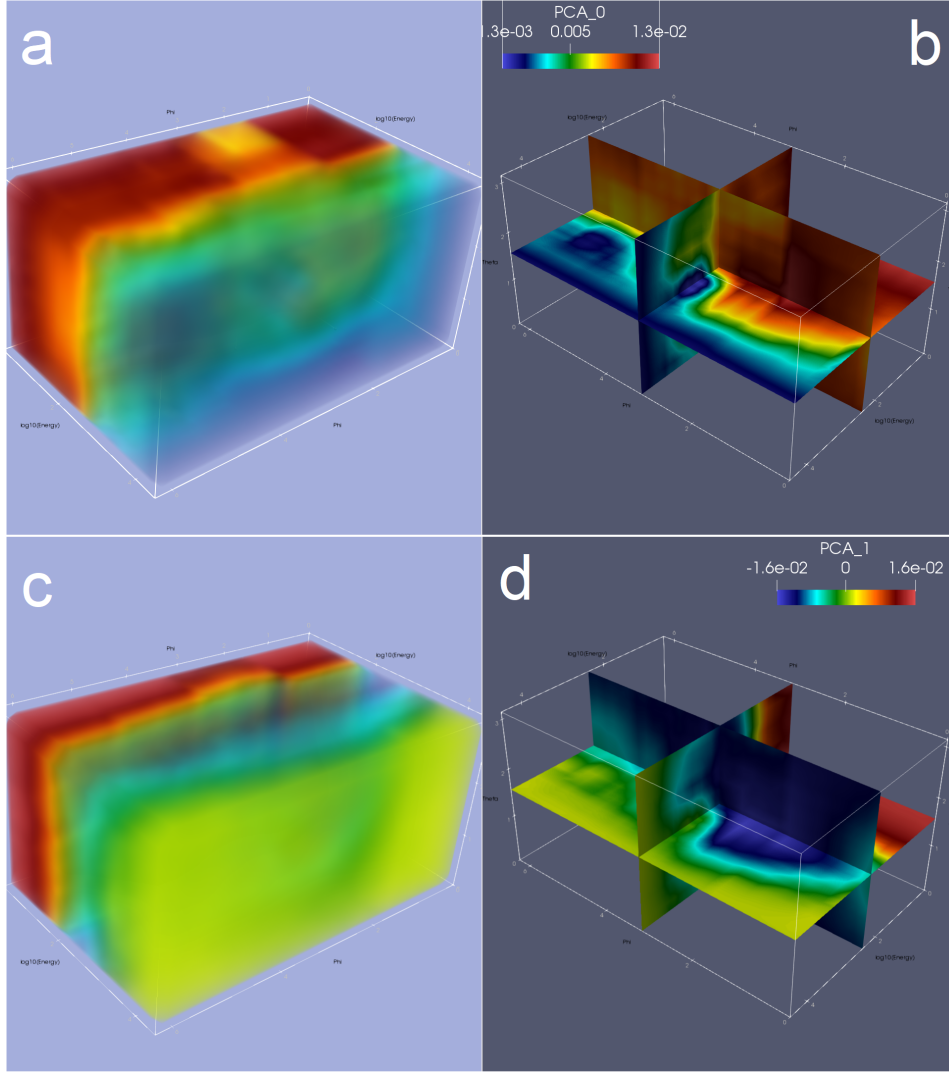


Figure 5. a, b) Volume rendering and slice cuts through the first PC computed from the human-labelled dataset, reshaped to $32 \times 16 \times 32$ array. Red color represents high variance, blue corresponds to low variance. c,d) Same for the second PC.

CNN predictions for each actual, human-labelled class, together with Figure 7, which presents the evaluation of the CNN performance on the test subset, show that all IF errors represent mixed states with either SW or MS. As IF, by definition, is the solar wind plasma contaminated by shock-reflected ions, these errors are to be expected, even in human-labelled sets. A possible approach for future studies might be not to separate IF out as a clean state, but define it as a mixture of other classes. One might also consider detecting the solar wind beam as an object in the 3D spectrogram.

After testing, the CNN was deployed to classify two months of FPI DIS data, Nov and Dec 2017. It appears that 98.7% of the labels are predicted with probability more than 0.7. As mixed classes are of most interest, we treat the regions with prediction probability less than 0.5 as unknown. The unknown/mixed regions constitute $\approx 0.04\%$ of all examples. We highlight these regions on the orbit of MMS with yellow circles (Figure 8). The majority of such mixed states are located on the MS/MSP and SW (IF)/MS boundaries, i.e., they may indicate the magnetopause and bow shock regions.

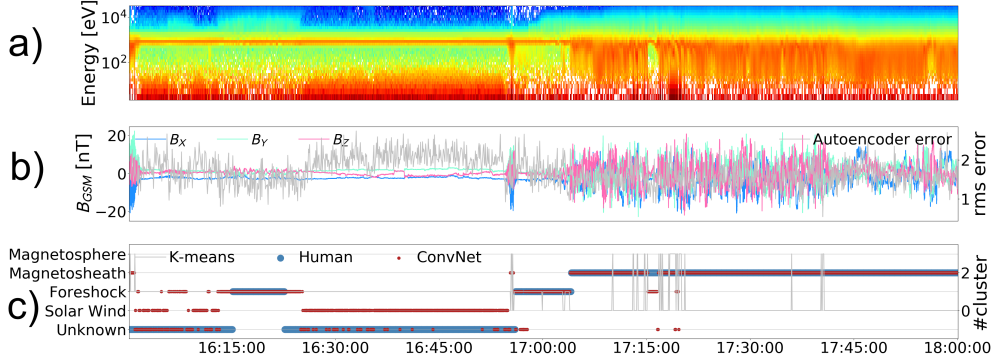


Figure 6. Observations on 2017.11.13 16:00 – 18:00. a) \log_{10} of the energy distribution integrated over ϕ, θ . b) Left axis, blue, green, pink: x, y, z components of the magnetic field $|B_{GSM}|$ measured by FGM; right axis, grey: mean-square error of the 3D-CAE. c) Human-made labels (blue circles) and classification results: red circles – CNN, grey line – index of the k-means cluster computed over the data compressed by the encoder.

Table 4. Confusion matrix for the CNN predictions on the reference dataset.

		Actual			
		SW	IF	MS	MSP
Predicted	SW	116776	199	3	0
	IF	665	12465	123	1
	MS	0	21	64425	0
	MSP	0	1	0	19258

Finally, automated classification of massive amounts of observational data allows to study correlations between different properties of different plasmas. For instance, by plotting labelled examples in the coordinates of the magnetic field $B_{z,GSM}$ and the distance to the Earth r_{GSE} (Figure 9), one could observe that only a few ‘Unknown’ examples point to the locations with strong negative B_z which are close to the Earth. These regions might signal magnetic reconnection events.

5 Conclusions

We present a method for automated detection of the plasma regions traversed by the MMS spacecraft in its dayside campaign. This technique is based on the ML classification of the ion energy spectrograms measured by the FPI DIS instrument and employs supervised learning with a 3D deep convolutional neural network (CNN). The CNN, trained on just a small subset (5%) of the human-labelled dataset (278,110 examples) predicts the correct label (plasma region) with 99.5% accuracy when applied to the whole dataset. The CNN is excellent at detecting the solar wind, magnetosheath, and magnetosphere, but has a $\approx 6\%$ chance to mistakingly treat a solar wind region as an ion foreshock region. This, however, is a result of the complex origin of the foreshock, which is a mixed plasma state containing signatures from other states.

The CNN could be used to detect the mixed/boundary regions, such as the bow shock or magnetopause. The latter points to the locations of magnetic reconnection events,

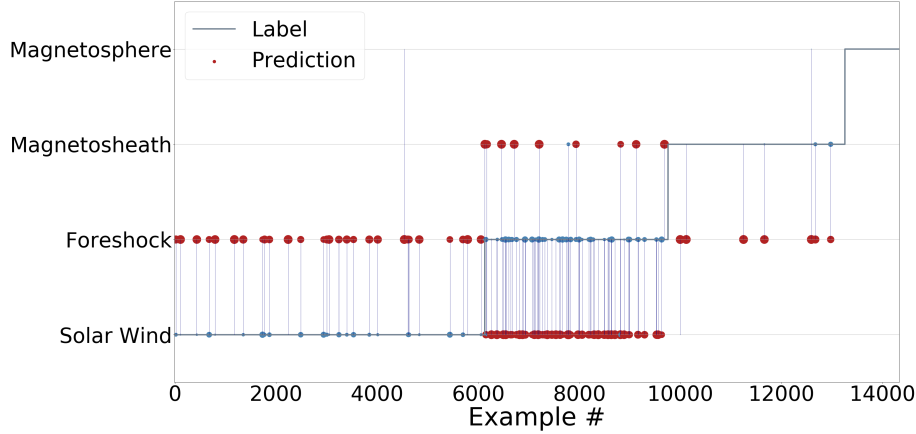


Figure 7. Predictions of the trained CNN for the test set. Grey line is the reference label. Red circles correspond to the wrong predictions. Blue circles represent the second most probable predictions for these examples. The sizes of the circles are proportional to the predicted probabilities.

the focus of the MMS mission. We have developed a software package which could be deployed in data centers and be used for automatic classification of observations, statistical analysis and visualization of the data.

We have applied the Principal Component Analysis to the observed dataset to find that the first two principal components (PCs) cover 50% of the explained variance in the data, but more than 500 PCs are needed to cover 80% of the variance. This result suggests that simple ML techniques might not be sufficient for classification of the 3D ion spectrograms.

We also tried to use a 3D convolutional autoencoder for unsupervised classification of the data and anomaly detection. However, the clustering computed over the compressed representation does not seem to reflect the physical separation of the plasma regions. We also did not succeed in developing an accurate anomaly detector based on the autoencoder. There is no apparent correlation between a high error of the data processed through the encoder, and any sort of a mixed state revealed by the observations.

Our work does not intend to present a comprehensive study of all possible ML approaches for automated classification of the MMS observations. However it offers an implementation that works and produces accurate results based on FPI DIS ion spectrogram data. Our work opens new possibilities for future research. First of all, more studies are needed to find a way to accurately distinguish the ion foreshock regions from the solar wind. It would be extremely useful to perform a statistical analysis of the mixed regions detected by the CNN, and figure out whether magnetic reconnection events could be found in those regions. There is a big potential in studying correlations of different plasma properties measured in different classes, predicted by the CNN.

References

- Ballard, D. H. (1987). Modular learning in neural networks. In *Proceedings of the sixth national conference on artificial intelligence - volume 1* (pp. 279–284). AAAI Press. Retrieved from <http://dl.acm.org/citation.cfm?id=1863696.1863746>

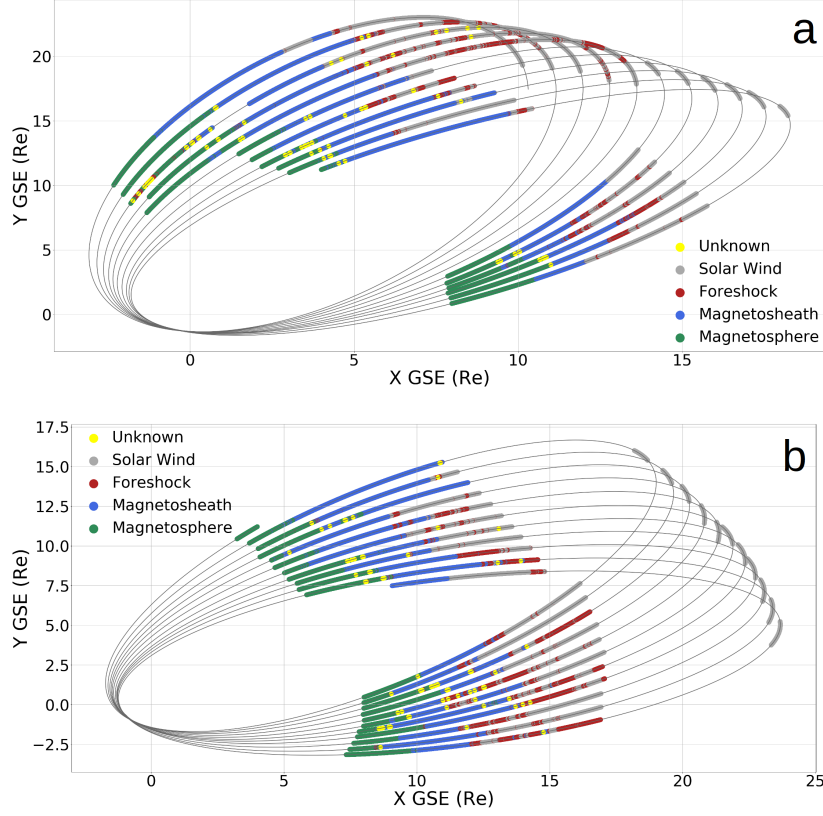


Figure 8. Predictions of the trained CNN for two months of observations: Nov 2017 (a) and Dec 2017 (b), plotted in the x_{GSE} and y_{GSE} coordinates. Color circles denote different regions, and the grey line shows the spacecraft trajectory.

- Burch, J. L., Moore, T. E., Torbert, R. B., & Giles, B. L. (2016, Mar 01). Magnetospheric multiscale overview and science objectives. *Space Science Reviews*, 199(1), 5–21. Retrieved from <https://doi.org/10.1007/s11214-015-0164-9> doi: 10.1007/s11214-015-0164-9
- Camporeale, E. (2019, Mar). The Challenge of Machine Learning in Space Weather Nowcasting and Forecasting. *arXiv e-prints*, arXiv:1903.05192.
- Fuselier, S. A., Lewis, W. S., Schiff, C., Ergun, R., Burch, J. L., Petrinec, S. M., & Trattner, K. J. (2016, Mar 01). Magnetospheric multiscale science mission profile and operations. *Space Science Reviews*, 199(1), 77–103. Retrieved from <https://doi.org/10.1007/s11214-014-0087-x> doi: 10.1007/s11214-014-0087-x
- Fuselier, S. A., Vines, S. K., Burch, J. L., Petrinec, S. M., Trattner, K. J., Cassak, P. A., ... Webster, J. M. (2017). Large-scale characteristics of reconnection diffusion regions and associated magnetopause crossings observed by mms. *Journal of Geophysical Research: Space Physics*, 122(5), 5466–5486. Retrieved from <https://agupubs.onlinelibrary.wiley.com/doi/abs/10.1002/2017JA024024> doi: 10.1002/2017JA024024
- Goodfellow, I., Bengio, Y., & Courville, A. (2016). *Deep learning*. MIT Press. (<http://www.deeplearningbook.org>)
- Hotelling, H. (1933). Analysis of a complex of statistical variables into principal components. *Journal of Educational Psychology*, 24, 417–441, 498–520.

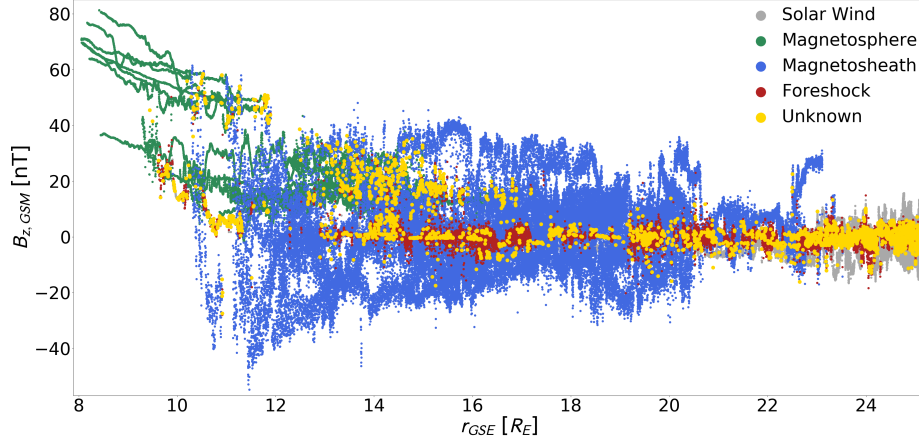


Figure 9. Dependence of B_z on the distance to the Earth for different regions for the Nov 2017 dataset.

- Jolliffe, I. (2002). *Principal component analysis*. Springer. Retrieved from https://books.google.se/books?id=_o1ByCrhjwIC
- LeCun, Y., Bengio, Y., & Hinton, G. (2015, May). Deep learning. *Nature*, 521(7553), 436-444. doi: 10.1038/nature14539
- Maturana, D., & Scherer, S. (2015, Sep.). Voxnet: A 3d convolutional neural network for real-time object recognition. In *2015 IEEE/RSJ International Conference on Intelligent Robots and Systems (IROS)* (p. 922-928). doi: 10.1109/IROS.2015.7353481
- Pearson, K. (1901). Liii. on lines and planes of closest fit to systems of points in space. *The London, Edinburgh, and Dublin Philosophical Magazine and Journal of Science*, 2(11), 559-572. Retrieved from <https://doi.org/10.1080/14786440109462720> doi: 10.1080/14786440109462720
- Piatt, S. (2019, May). Large-Scale Statistical Survey of Magnetopause Reconnection. *arXiv e-prints*, arXiv:1905.11359.
- Pollock, C., Moore, T., Jacques, A., Burch, J., Gliese, U., Saito, Y., ... Zeuch, M. (2016, Mar 01). Fast plasma investigation for magnetospheric multiscale. *Space Science Reviews*, 199(1), 331-406. Retrieved from <https://doi.org/10.1007/s11214-016-0245-4> doi: 10.1007/s11214-016-0245-4
- Russell, C. T., Anderson, B. J., Baumjohann, W., Bromund, K. R., Dearborn, D., Fischer, D., ... Richter, I. (2016, Mar 01). The magnetospheric multiscale magnetometers. *Space Science Reviews*, 199(1), 189-256. Retrieved from <https://doi.org/10.1007/s11214-014-0057-3> doi: 10.1007/s11214-014-0057-3